Ion Temperature Imaging of the Earth's Magnetosphere

Earl E. Scime, Anna M. Zaniewski, Ruth M. Skoug, Michelle Thomsen, and Craig J. Pollock

***Abstract*—Detection of neutral atom emission from hot plasmas has evolved to the point where it is now possible to image hot plasmas in neutral atom emission. In this paper, we review the qualitative and quantitative spatially resolved information that can be obtained from neutral atom images, e.g., hot ion transport and ion temperatures. A challenging aspect of neutral atom imaging of the earth's quiet time magnetosphere is that the combination of small neutral fluxes and spacecraft motion necessitates the development of algorithms capable of summing neutral emission obtained from different vantage points over many months to obtain statistically significant images. The image summing algorithm and typical summed images are also presented in this work.**

***Index Terms*—Magnetic storms, magnetosphere, plasma properties.**

I. Neutral Atom Imaging and Instrument Description

In the 1980s, Roelof demonstrated that energetic particle measurements inadvertently obtained during cusp transits by the IMP 7/8 and ISEE-1 spacecraft were consistent with the detection of energetic neutral atoms produced by charge exchange collisions between magnetospheric plasma and the earth's geocorona [1]. After he showed that the neutral atom emission could be used to create neutral atom images that reflected the spatial structure of the magnetospheric plasma [2], the space plasma community embraced the concept of neutral atom imaging. The earth's magnetospheric plasma coexists with the diffuse, very low temperature, neutral atom atmosphere (the geocorona) that surrounds the earth [3], [4]. In regions where the geocorona coexists with hot plasma, fast ions undergo charge exchange collisions with the background neutral atoms; producing a cold ion and an energetic neutral atom with the same velocity vector as the original ion. The cross section for charge exchange collisions between ions and neutrals is a strong function of center of mass energy and is well known from laboratory measurements [5]. In laboratory plasma experiments, where neutral atom measurements were first employed [6], this type of neutral atom measurement is called a charge exchange measurement. The typically peaked ion temperature profiles of laboratory plasmas yield a neutral atom energy spectrum from which the ion temperature is easily extracted if the plasma is optically thin [7].

Since 1987, a variety of methods for neutral atom imaging have been considered in the scientific literature and instruments based on some of the proposed techniques have flown in space. Gruntman's review of the history of space-based neutral atom detection, neutral atom imaging, and the different techniques that can be used to image neutral atoms is an excellent resource for readers interested in an in-depth discussion of neutral atom imaging [8]. Only a brief review of the essential elements of the medium energy (1–70 keV) neutral atom imager used to obtain the data used in this work is presented here. Detection and imaging of neutrals at energies less than 40 keV, the energy range at which much of the inner magnetospheric and plasmasheet neutral atom emission occurs [9]–[11], is technologically challenging because ultraviolet (UV) blocking foils cannot be used to eliminate UV from triggering low-energy particle detectors [8]. In 1991, Gruntman suggested direct detection of neutral atoms with a position sensitive detector while blocking the intense background photon flux with a filtering structure that permitted the passage of atoms but not ultraviolet photons. Free-standing gold gratings with nominal 150-nm bars and 50-nm gaps have roughly 10^{-6} UV transmissions and 10^{-1} atom transmissions [12], [13]; ideal for use as UV blockers in a direct detection neutral atom imager. The medium energy neutral atom (MENA) imager launched aboard the Imager for Magnetopause-to-Aurora Global Exploration (IMAGE) spacecraft [14] in 2000 is a grating-based, direct detection neutral atom imager [15]. MENA is composed of three sensor heads, each of which functions as an independent wide slit camera (Fig. 1). Each head provides a one-dimensional image of incident ENAs; the second imaging direction is obtained from the spacecraft spin. As neutral atoms transverse the instrument, they enter through a charged particle deflecting collimator. The neutral atoms then pass through a UV blocking grating and the fraction that pass through the grating then transit a thin carbon foil. The passage of a neutral atom through the carbon foil typically liberates one or more secondary electrons. The electrons are then accelerated to the microchannel plate detector Start segment. When the atom arrives in the Stop segment of the detector, the incident angle and time-of-flight (TOF) are determined using the corresponding Start and Stop data. The trajectory and time-of-flight measurements are then combined to calculate the neutral atom speed [15], [16]. A coincidence requirement for valid events reduces the background from light and penetrating radiation. On a statistical basis, the fraction of different ENA species can, in principle, be determined from detector pulse heights, but such measurements are not routinely

Manuscript received August 22, 2004; revised October 25, 2004. This work was supported by West Virginia University and the Southwest Research Institute under NASA Contract NAS5-96 020. The work at Los Alamos National Laboratory was performed under the auspices of the U.S. Department of Energy.

E. E. Scime and A. M. Zaniewski are with the Department of Physics, West Virginia University, Morgantown, WV 26506-6315 USA.

R. Skoug and M. Thomsen are with the Los Alamos National Laboratory, Los Alamos, NM 87544 USA.

C. J. Pollock is with the Space Science and Engineering Division, Southwest Research Institute, San Antonio, TX 78228 USA.

Digital Object Identifier 10.1109/TPS.2005.844597

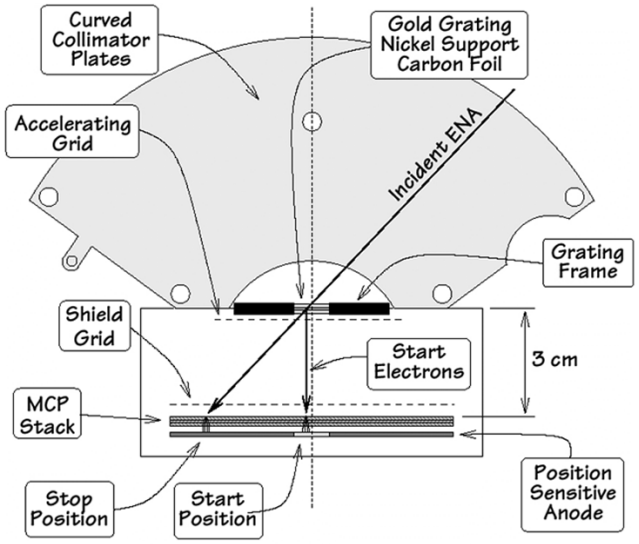

Fig. 1. Essential elements of the MENA imager: high-voltage collimators for charged particle rejection (with $\pm 55^\circ$ polar acceptance and $\pm 2^\circ$ azimuthal acceptance); UV blocking gold gratings on a nickel frame; start pulse carbon foil attached to gold gratings; electron acceleration and secondary suppression grids; and position sensitive detector for neutrals and electrons. Figure adapted from [16].

made. On-board the spacecraft, TOF, Start, and Stop positions are processed into energy-resolved images and telemetered to the ground along with direct-event data. The on-board image data are processed using an approximate calibration algorithm and consist of images separated into only five discrete energy bands. The direct-event data include the Start, Stop, and TOF values for each event, thus the direct-event data have significantly higher energy resolution. For energy spectra analyses, such as ion temperature measurements, the better energy resolution of the direct-event data is preferable. Telemetry bandwidth restrictions limit the number of direct-events that can be transmitted during each spacecraft spin and thus the direct-event data are limited to a maximum count rate and their azimuthal resolution restricted to 8° during intervals of intense geomagnetic activity. A separate measure of the total number of events counted per spacecraft spin interval enables scaling of the direct-event rate data to the more complete on-board count rate data.

The entire MENA instrument, including power supplies, has a mass of 13.2 kg and consumes 22.5 W of power [15]. The azimuthal, "spin," angular coverage of the instrument is 360° with 4° resolution determined by the angular acceptance of the collimating structure. The polar, "imaging," coverage spans 160° with a typical imaging resolution of 4°. Each individual head has a polar imaging range of only 120°, but each head is offset by 20° to compensate for the 20° blind spot in the center of each head (due to an inability to distinguish between electrons and neutrals striking the start detection region of the imaging microchannel plate stack). The microchannel plate detector consists of a custom z stack of Hamamatsu microchannel plates (MCP) in front of a position sensitive anode. The MCPs provide large area (72 mm $\times$ 90 mm), relatively high resistance ($\sim$100 M-μ per plate), high gain due to channels with 60:1 length-to-diameter ratio. The MCPs also operate with low noise (<1 cm^{-2} s^{-1}), very low rate of after-pulsing as required for the TOF work, and excellent uniformity ($<10\%$ variations over their surface). The 1–70-keV/nucleon energy range and geometric factor of 0.1 cm^{2}sr of MENA is adequate to detect ENAs from the inner magnetosphere, ring current, and plasma sheet.

II. Image Analysis

Raw energetic neutral atom flux images, flux versus spin and imaging angle, are obtained from the three neutral atom imagers [15], [17], [18] aboard the IMAGE spacecraft every two minutes (every spin). The raw time and energy resolved images are used to qualitatively investigate dynamic magnetospheric processes such as plasma injections during large geomagnetic storms [9] and the dramatic increase in plasmasheet density that appears to preceed large storms [19]. The details of the energy spectra of the neutral flux, as well as the transport of ions in the inner magnetosphere, are now routinely used to determine magnetospheric electric fields [20] and in conjunction with sophisticated analysis techniques, can be used to determine the spatial distribution of ions in the equatorial plane [21]. However, even without inverse modeling techniques, quantitative information, specifically ion temperatures, can be extracted from neutral atom images.

For energetic neutral atom emission along a given viewing direction, the contribution to the high-energy portion of the energy spectrum from a hot space plasma is dominated by emission from the hottest region along the line of sight. The high-energy portion of the neutral atom energy spectrum, $F(E)$, generated via charge exchange collisions for a Maxwellian ion distribution of temperature T, is given by [7]

$$F(E)dE \approx C\sigma(E)EdE \left(\frac{n_o(r)n_i(r)e^{-E/T(r)}}{\sqrt{2m_i\pi^3 T(r)^3}} \right)_{r=x} \times e^{-\int_x^\alpha \alpha(l)\,dl} \quad (1)$$

where $F(E)$ is in units of #/cm^2·s, C is a constant that accounts for the geometrical viewing properties of the instrument and the column line-of-sight integration over the hottest region (located at some point x along the line-of-sight). The hottest region is assumed to be of constant temperature and therefore the column integration of the neutral emission region yields a constant multiplicative factor. $T(r=x), n_o(r=x)$, and $n_i(r=x)$ are the ion temperature, neutral density, and ion density at the same location, respectively. m_i is the ion mass. $\sigma(E)$ is the energy dependent charge exchange cross section [5] between neutrals and ions of energy E and the integral over $\alpha(l)$, where $\alpha(l)$ is the mean number of collisions per unit length, accounts for the reduction of neutral flux originating from the location of the hottest region due to additional collisions or ionization as the neutrals travel from point x to the instrument located at point a. Outside of the plasmapause, the ion [22] and neutral densities [4] are low enough that the magnetosphere is optically thin to energetic neutral atom emission. Thus

$$\frac{F(E)dE}{\sigma(E)EdE} \approx C \left(\frac{n_o(x)n_i(x)}{\sqrt{2m_i\pi^3 T(x)^3}} \right) e^{-E/T(x)}. \quad (2)$$

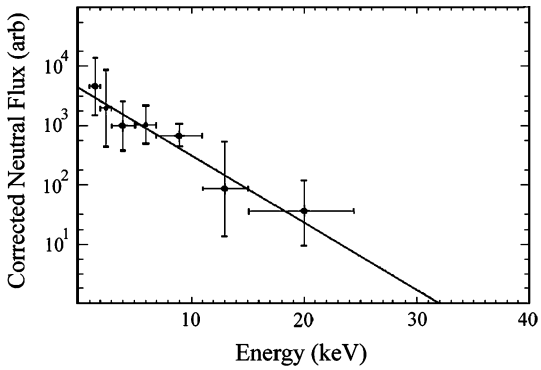

Fig. 2. Logarithm of the corrected neutral atom flux averaged over thirty spacecraft spins versus neutral energy and a fit to the data using (2).

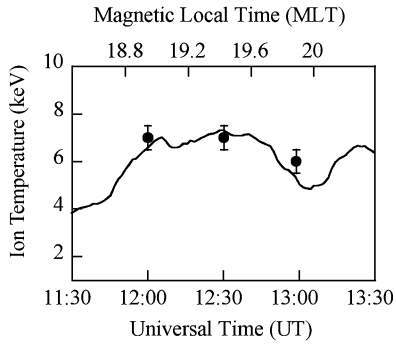

Fig. 3. Ion temperature versus time obtained from the 1994-84 Magnetospheric Plasma Analyzer instrument (solid line) in geosynchronous orbit and in the field of view of the MENA instrument [24]. Data have been smoothed with a twenty-minute boxcar average for consistency with the MENA image data. Remotely measured ion temperatures from MENA data (solid circles) with ± 0.5 eV error bars at 12:00, 12:30, and 13:00 UT.

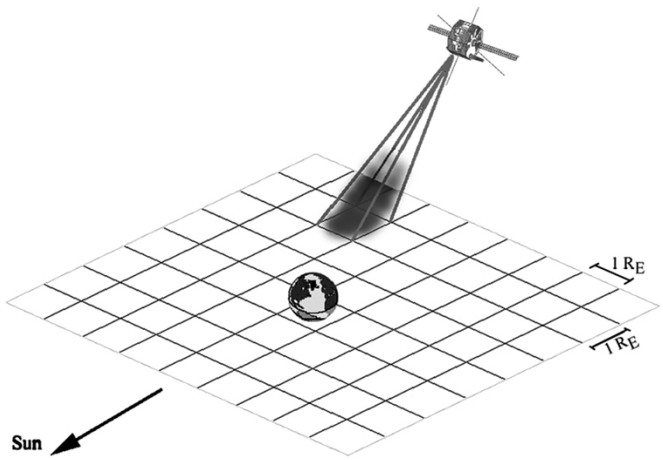

Fig. 4. Mapping geometry used to combine MENA data from different times of the year and from different regions of individual orbits.

This analysis assumes the neutral atom fluxes are due to charge exchange between protons and neutral hydrogen. The energy bins of the MENA instrument are based solely on time-of-flight measurements, and thus the mass (and energy) of the neutral atoms is not known.

A standard least squares linear fit with (2) to determine the slope of the natural logarithm of the correct neutral flux as a function of energy yields the peak ion temperature along the line of sight for statistics data sorted into seven energy bins and corrected for the energy-dependent charge exchange cross section. An example spectrum is shown in Fig. 2 for a single imaging line-of-sight (imaging pixel). Although the MENA instrument is capable of measuring neutral energies of up to 70 keV/nucleon, energies above 25 keV were excluded from the analysis presented here to avoid complications arising from background counts and known instrumental artifacts. As the linear fit to the natural logarithm of the charge exchange corrected neutral flux shown in Fig. 2 demonstrates, the spectrum is remarkably Maxwellian-like throughout the entire 1–25-keV energy range. The Maxwellian nature of the entire neutral energy spectrum suggests either a strong ion temperature gradient along the line-of-sight (i.e., a very spatially localized region of high ion temperature) or that the ion temperature is nearly homogeneous along the line-of-sight. Without multiple lines-of-sight through these plasma regions, neutral atom emission measurements cannot distinguish between the two possible explanations. The statistical error in each ion temperature determination is calculated based on the uncertainties in the energies of each energy bin and on the statistical uncertainty in the number of counts in each energy bin.

During storm times, the remotely determined ion temperatures in a single imaging pixel are consistent in both magnitude and temporal evolution with *in situ* ion temperatures obtained by equatorial spacecraft located on the imaging line-of-sight corresponding to that pixel (see Fig. 3 for a comparison of MENA and *in situ* magnetospheric plasma analyzer (MPA) [23] data) [24]. During magnetospherically quiet intervals, the neutral fluxes are too small to extract either qualitative or quantitative information from the images. To improve the precision of the ion temperature measurements, either the individual temperature measurements or the raw neutral fluxes (followed by temperature analysis) can be averaged over time. Averaging the raw fluxes over one hour intervals is more than sufficient to obtain statistically significant ion temperature measurements for geomagnetically active intervals (often only integration times of a few minutes can be employed) and longer integrations are required for geomagnetically quiet intervals [25]. Because the IMAGE spacecraft is in a highly elliptical orbit and MENA image pixels are typically $4^\circ \times 4^\circ$, significant blurring of small scale structures due to the motion of the spacecraft can occur on one-hour time scales. In addition, the location of the sun-earth line moves in the MENA image plane throughout the IMAGE mission due to the precession of the line of apsides and motion of the earth around the sun, i.e., the viewing geometry changes significantly because of seasonal changes and orbital precession.

To average images over intervals longer than one hour, we project each line of sight to a $1R_E \times 1R_E$ fixed grid placed in the equatorial plane (Fig. 4). The neutral fluxes measured along each line of sight are then binned according to which grid sector the line of sight intersects. To account for the different lengths of time that each grid sector is in view, the total flux in each grid sector was then normalized by the number of times that particular grid sector was viewed by the MENA instrument. Similar mapping techniques have been used previously for ENA image data from the Polar spacecraft [26]. However, here the data are mapped to the same fixed grid regardless of the season

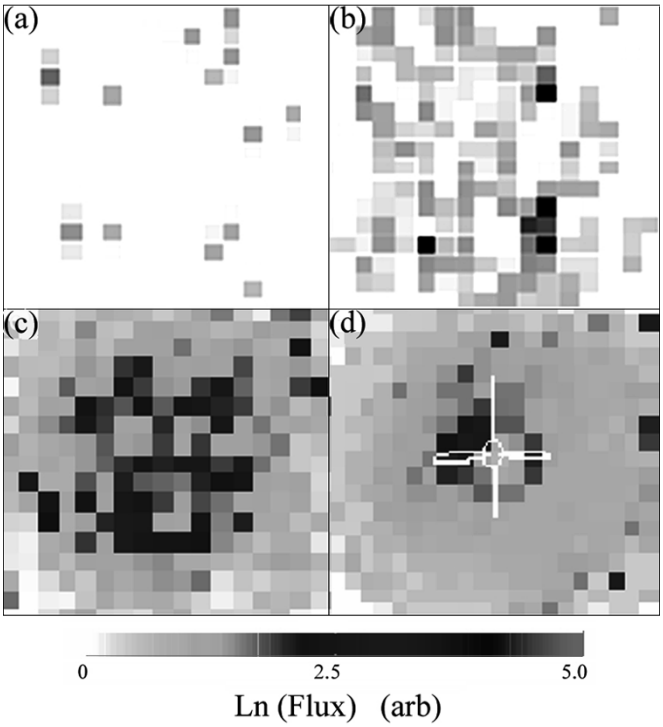

Fig. 5. Quiet time (Dst $\sim$ 0) magnetospheric 1–2 keV neutral atom flux (a) for a single two-minute acqusition, (b) averaged 10 images, (c) averaged over 80 images, and (d) for 27–60 keV neutral atom flux averaged over 1028 images.

of the orbit or the location of the spacecraft. The fluxes have been projected to the equatorial plane and aligned so that the sun is to the right and the earth in the center in each image. $L = 2$ and $L = 4$ representative magnetic field lines are shown centered on the earth.

The image sequence shown in Fig. 5 demonstrates the improvement in the signal-to-noise of neutral atom images obtained as our flux mapping algorithm is applied to larger and larger sets of images acquired during intervals of negligible geomagnetic activity (disturbance storm time index, Dst, $\sim$0). A single two minute integrated image is shown in Fig. 5(a). An average over 10 images is shown in Fig. 5(b) and an 80 image average ($\sim$2.5 hours) is shown in Fig. 5(c). In the 80 image average, the neutral flux is clearly most intense in the center of the image (around the earth) and discrete structures are visible. An averaged image based on 1028 individual images, over 34 hours of data, is shown in Fig. 5(d). In all of the images in Fig. 5, the sun is to the right, the earth is in the center of the image, and the view is from above the magnetic north pole, i.e., the image data is mapped according to magnetic local time (MLT).

The ring current, with a typical scale size of a single pixel and a pre-midnight enhancement, is clearly evident in Fig. 5(d) between 2 and 4 R_E in this equatorial projection. The ring current is 1 grid element in size $(1R_E)$ centered on $3R_E$ with a discrete, macroscopic feature in the pre-midnight sector. In situ measurements indicate that the quiet time ring current consists primarily of protons, is located between 2 and 5 R_E, and has a peak ion flux between 50 and 100 keV [27]. Because the images used in Fig. 5(d) were obtained from intervals evenly distributed around the earth's orbit around the sun, there is no bias in the average image due to seasonal effects or viewing geometry.

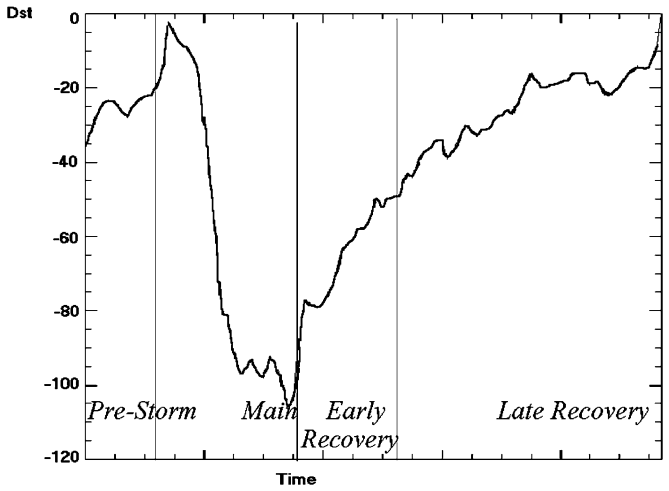

Fig. 6. Intense geomagnetic storm from November 1, 2001 divided in prestorm, main, early recovery, and late recovery phases based upon the Dst profile criteria used in this study.

III. Superposed Epoch Analysis of a Geomagnetic Storm

To obtain reliable ion temperature images with sufficient time resolution to investigate the temporal evolution of a large geomagnetic disturbance, images from well-defined stages of many storms can be averaged together. During a geomagnetic storm, material from the plasma sheet is driven into the near-earth magnetosphere, enhancing the ring current. Since the majority of neutral atoms detected by the MENA instrument originate in the ring current, Dst (the value of which is highly dependent on the strength of the ring current) is an appropriate index by which to quantify storm strength and phase as it relates to neutral atom emission [28], [29]. Each storm had a minimum Dst of at least -50 and the storms were divided into phases based on their Dst profile: prestorm, main, early recovery, and late recovery (Fig. 6).

The evolution of the remotely measured ion temperatures averaged over thirty storms between May 2000 and March 2002 is shown in Fig. 7. In the lower right hand corner of each image is a legend that indicates the orientation of the spacecraft field of view for every interval used to generate the summed image. The white arrows point along the spacecraft line of sight. Since the sun is to the right in each summed image, there should always be a gap in image coverage from roughly 45° to 135° as measured from the top of the image because the MENA instrument is turned off when both the magnetosphere and the sun are in the instrument's field of view. For Fig. 7(a), the prestorm image, the seasonal coverage is nearly complete as evidenced by the uniformity of coverage indicated in the field of view legend. The prestorm phase is relatively featureless in MLT, with ion temperatures of 2–3 keV throughout the inner magnetosphere. During the main phase, the magnetosphere generally heats up to temperatures of about 7 keV and the slightly hotter ring current is visible around 5–6 R_E. During the early recovery and late recovery phases, the ion temperature in the dawn region is slightly lower then in the noon, dusk, and midnight sectors of the ring current. Recently developed models that predict dawn-dusk

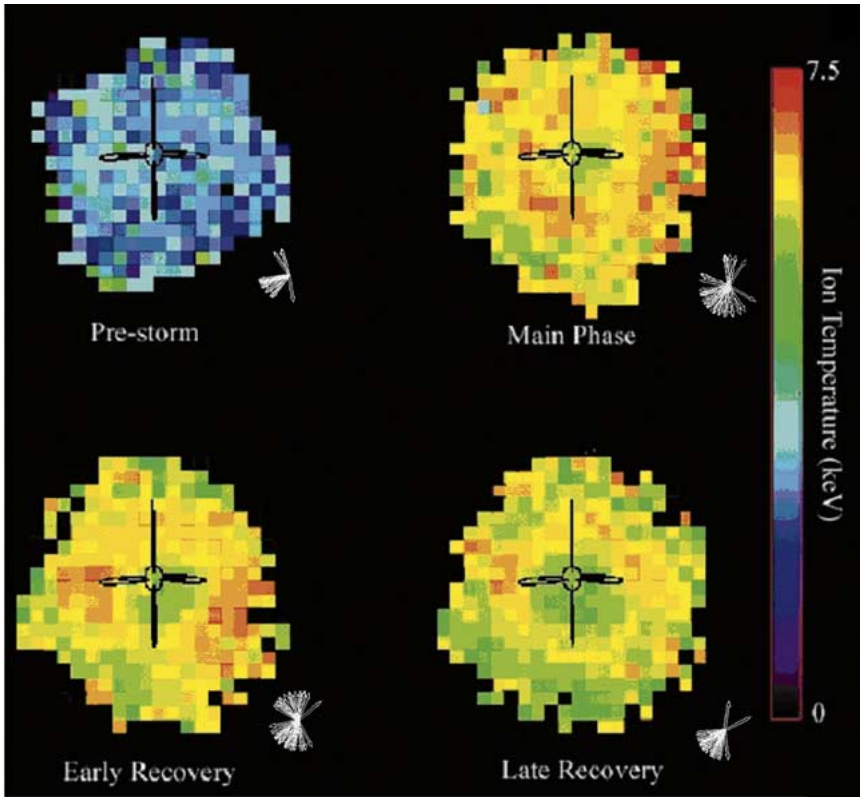

Fig. 7. Prestorm, main phase, early recovery, and late recovery ion temperature images averaged over 30 different storms. Field of view legend (in white) to the lower right of each image is a superposition of all the lines of sight used in each image.

temperature asymmetries suggest that the temperature asymmetries result from the preferential grad-B drift of energetic ions toward the dusk region [30], [31]. During late recovery, the bulk of the magnetosphere cools to around 5 keV, consistent with a loss of energetic ions through charge exchange, Coulomb interactions or other loss processes.

IV. Discussion

These results demonstrate that magnetospheric ion temperatures can be remotely determined through charge exchange analysis. Through long term averaging, even the quiet time magnetosphere can be imaged in neutral atoms. Combining a superposed epoch analysis of many storms with a new image summing algorithm enables the construction of time and spatially resolved ion temperature images of the terrestrial magnetosphere. For neutral energies of approximately 27–60 keV, the quiet time magnetosphere is sufficiently reproducible that single pixel structures, i.e., the quiet time ring current can be imaged if enough data are available. Because no two geomagnetic storms are identical, the summed storm-time images shown in Fig. 7 may include storms of substantially different characteristics even though the intervals all meet the same Dst temporal criteria. In future work, the storms will be further differentiated on the basis of additional criteria to provide more homogenous sets of storm images for subsequent summing.

References

[1] E. C. Roelof, D. Mitchell, and D. Williams, "Energetic neutral atoms (E $\sim$ 50 keV) from the ring current: IMP 7/8 and ISEE 1," *J. Geophys. Res.*, vol. 90, p. 10 991, 1985.

[2] E. C. Roelof, "Energetic neutral atom image of a storm-time ring current," *Geophys. Res. Lett.*, vol. 14, p. 652, 1987.

[3] N. Ostgaard, S. B. Mende, H. U. Frey, G. R. Gladstone, and H. Lauche, "Neutral hydrogen density profiles derived from geocoronal imaging," *J. Geophys. Res.*, vol. 108, pp. SMP18-1–SMP18-12, 2003.

[4] R. L. Rairden, L. A. Frank, and J. D. Craven, "Geocoronal imaging with dynamics explorer," *J. Geophys. Res.*, vol. 91, p. 13 613, 1986.

[5] R. L. Freeman and E. M. Jones, "Atomic Collision Processes in Plasma Physics Experiments,", vol. 137, Culham Laboratory Report CLM-R, 1974.

[6] V. V. Afrosimov *et al.*, "Multichannel energy and mass analyzer for atomic particles," *Sov. Phys. Tech. Phys.*, vol. 20, p. 33, 1975.

[7] I. H. Hutchinson, *Principles of Plasma Diagnostics*, Cambridge, U.K.: Cambridge Univ. Press, 1987.

[8] M. Gruntman, "Energetic neutral atom imaging of space plasmas," *Rev. Sci. Instrum.*, vol. 68, p. 3617, 1997.

[9] C. J. Pollock *et al.*, "First medium energy neutral atom images of the earth's magnetosphere during substorms and storm-time," *Geophys. Res. Lett.*, vol. 28, p. 1147, 2001.

[10] D. T. Young, "Near-equatorial magnetospheric particles from $\sim$1 eV to $\sim$1 MeV," *Rev. Geophys.*, vol. 21, p. 402, 1983.

[11] K. R. Moore *et al.*, "Low energy neutral atom emission from the earth's magnetosphere," *Opt. Eng.*, vol. 33, p. 342, 1994.

[12] E. E. Scime *et al.*, "Extreme ultraviolet polarization and filtering with gold transmission gratings," *Appl. Optics*, vol. 34, p. 648, 1995.

[13] M. M. Balkey *et al.*, "Effects of slit width on VUV transmission through sub-micron period, free-standing, transmission gratings," *Appl. Optics*, vol. 37, p. 5087, 1998.

[14] J. L. Burch, "IMAGE mission overview," *Space Sci. Rev.*, vol. 91, p. 1, 2000.

[15] C. J. Pollock *et al.*, "Medium energy neutral atom (MENA) imager for the IMAGE mission," *Space Sci. Rev.*, vol. 91, p. 113, 2000.

[16] M. G. Henderson *et al.*, "Calculation of IMAGE/MENA geometric factors and conversion of images to units of integral and differential flux," *Rev. Sci. Instrum.*, vol. 76, 2005.

[17] D. G. Mitchell *et al.*, "High energy neutral atom (HENA) imager for the IMAGE mission," *Space Sci. Rev.*, vol. 91, p. 67, 2000.

[18] T. E. Moore, "Low energy neutral atoms in the magnetosphere," *Geophys. Res. Lett.*, vol. 28, p. 1143, 2001.

[19] D. J. McComas *et al.*, "Filling and emptying of the plasma sheet: Remote observations with 1–70 keV energetic neutral atoms," *Geophys. Res. Lett.*, vol. 29, p. 36, 2002.
[20] P. C. Brandt *et al.*, "Global ENA observations of the storm main-phase ring current: Implications for skewed electric fields in the inner magnetosphere," *Geophys. Res. Lett.*, vol. 29, p. 15, 2002.
[21] J. D. Perez *et al.*, "Initial ion equatorial pitch angle distributions from medium and high energy neutral atom images obtained by IMAGE," *Geophys. Res. Lett.*, vol. 28, p. 1155, 2001.
[22] M. Kivelson and C. T. Russell, *Introduction to Space Physics*. New York, NY: Cambridge University Press, 1995.
[23] S. J. Bame *et al.*, "Magnetospheric plasma analyzer for spacecraft with constrained resources," *Rev. Sci. Instrum.*, vol. 64, p. 1026, 1993.
[24] E. E. Scime *et al.*, "Ion heating in the terrestrial magnetosphere during substorms and storm-time: MENA observations," *Geophys. Res. Lett.*, vol. 29, 2002. 10.1029/2001GL013 994.
[25] E. E. Scime, "Charge exchange imaging of space plasmas," *Rev. Sci. Instrum.*, vol. 75, p. 3526, 2004.
[26] G. D. Reeves and M. G. Henderson, "The storm-substorm relationship: Ion injections in geosynchronous measurements and composite energetic neutral atom images," *J. Geophys. Res.*, vol. 106, p. 5833, 2001.
[27] I. A. Daglis *et al.*, "The terrestrial ring current: Origin, formation, and decay," *Rev. Geophys.*, vol. 37, p. 407, 1999.
[28] Y. Ebihara *et al.*, "On the global production rates of energetic neutral atoms (ENA's) and their association with the Dst index," *Geophys. Res. Lett.*, vol. 26, p. 2929, 1999.
[29] A. M. Jorgensen *et al.*, "Global energetic neutral atom (ENA) measurements and their association with the Dst index," *Geophys. Res. Lett.*, vol. 24, p. 3173, 1997.
[30] M. C. Fok, T. E. Moore, J. U. Kozyra, G. C. Ho, and D. C. Hamilton, "Three-dimensional ring current decay model," *J. Geophys. Res.*, vol. 100, pp. 9619–9632, 1995.
[31] Y. S. Ebihara and M. Ejiri, "Simulation study on fundamental properties of the storm-time ring current," *J. Geophys. Res.*, vol. 105, pp. 15 843–15 859, 2000.

Earl E. Scime received the B.S. degrees in physics and applied mathematics from Florida State University, Tallahassee, in 1987 and the Ph.D. degree in experimental plasma physics from the University of Wisconsin, Madison, in 1992.

He is Chair and Professor of Physics at West Virginia University in Morgantown, WV. He From 1992 to 1994, he was a Department of Energy Distinguished Postdoctoral Fellow in the Space Plasma Physics group at Los Alamos National Laboratory, Los Alamos, NM. In 1995, he moved to West Virginia University. His research interests include charge exchange imaging of high-temperature plasmas, the mechanisms of ion heating in space and laboratory plasmas, spacecraft charging, helicon plasma source development, laser induced fluorescence diagnosis of laboratory plasmas, plasma thrusters, double layers, plasma processing, and the theory of instabilities driven by flow shear and thermal anisotropy.

Anna M. Zaniewski is currently working toward the B.S. degree in physics, minoring in English and Africana studies at West Virginia University (WVU), Morgantown.

Her research while at WVU has focused on neutral atom imaging and image processing techniques to correct for changes in viewing geometry due to spacecraft motion and orbital precession.

Ms. Zaniewski is a recipient of a West Virginia University Bucklew Scholarship and a Goldwater Scholarship.

Ruth M. Skoug received the B.A. degrees in physics and mathematics from St. Olaf College, Northfield, MN, in 1989, and the M.S. degree in physics and the Ph.D. degree in physics from the University of Washington, Seattlem in 1991 and 1995, respectively.

She is a Technical Staff Member in the Space Science and Applications group at Los Alamos National Laboratory (LANL), Los Alamos, NM. She joined LANL in 1997. She From 1995 to 1997, she was a Postdoctoral Research Associate at the University of Washington. She has participated in two auroral sounding rocket projects, and developed and built a search coil antenna to detect very-low-frequency waves from a sounding rocket platform. She is a coinvestigator on the NASA Ulysses and TWINS missions. Her research interests include solar wind variability and its implications for space weather forecasting, solar wind suprathermal electron distributions, interplanetary coronal mass ejections, and global imaging of the magnetosphere.

Michelle Thomsen received the B.A. degree in physics from Colorado College, Colorado Springs, in 1971, and the M.S. and Ph.D. degrees in physics from the University of Iowa, Iowa City, in 1974 and 1977, respectively.

She is a Technical Staff Member in the Space Science and Applications group in Los Alamos National Laboratory, Los Alamos, NM. Her major area of interest is magnetospheric physics, with particular emphasis on the analysis and interpretation of spacecraft data. She has held postdoctoral research positions at the University of Iowa and the Max Planck Institute for Aeronomy. She has been a Staff Member at Los Alamos since 1981. She was a Space Physics Team Leader from 1998 to 2000 and was a Visiting Professor of Physics at Colorado College during 2002. She is an author or coauthor of over 280 refereed publications.

Dr. Thomsen is currently the Secretary of AGU/SPA-Magnetospheres section and chair, NASA sun-earth Connections Subcommittee. She has received the following honors: Journal of Geophysical Research Editor's Citation for Excellence in Refereeing, 1983, 1991; Distinguished Alumni Award, University of Iowa, 1985; Honorary Doctorate in science, Colorado College, 1992; Los Alamos National Laboratory Fellow, 1997; AGU Fellow, 2001.

Craig J. Pollock received the B.S. degrees in physics from Siena College, Loudonville, NY, in 1980 and the Ph.D. degree in physics from the University of New Hampshire, Durham, in 1987.

He is a Staff Scientist within the Space Science and Engineering Division at Southwest Research Institute, San Antonio, TX. From 1987 to 1989, he was a National Research Council Postdoctoral Fellow in the Space Plasma Physics group at Marshall Space Flight Center, before joining that group as a NASA employee in 1989. In 1996, he moved to Southwest Research Institute. His research interests include experimental observation of plasmas in the environments of the earth and other solar system bodies, the dynamics and configuration of the earth's magnetosphere, sources of magnetospheric plasmas, ion heating mechanisms operative in space, spacecraft charging, and the effects of spacecraft charging on plasma measurements.